UNICA IRIS Institutional Research Information System

This is the Author's submitted manuscript version of the following contribution:

Tocco D., Chelazzi D., Mastrangelo R, Casini A., Salis A.*, Fratini E.*, Baglioni P., Conformational changes and location of BSA upon immobilization on zeolitic imidazolate frameworks, Journal of Colloid and Interface Science, 641 (2023) 685-694.

The publisher's version is available at:

https://doi.org/10.1016/j.jcis.2023.03.107

When citing, please refer to the published version.

This full text was downloaded from UNICA IRIS https://iris.unica.it/

Conformational changes and location of BSA upon immobilization on zeolitic imidazolate frameworks

Davide Tocco,[1,2] *David Chelazzi,*[2] *Rosangela Mastrangelo,*[2] *Andrea Casini,*[2] *Andrea Salis,*[1,]* *Emiliano Fratini,*[2,]* *Piero Baglioni*[2]

[1] Department of Chemical and Geological Sciences, University of Cagliari & CSGI, Cittadella Universitaria, S.S. 554 bivio Sestu, 09042 Monserrato, CA, Italy

[2] Department of Chemistry "Ugo Schiff", University of Florence & CSGI via della Lastruccia 3, Sesto Fiorentino (FI), I-50019, Italy

E-mail: asalis@unica.it (AS); emiliano.fratini@unifi.it (EF)

Abstract

The location and the conformational changes of proteins/enzymes immobilized within Metal Organic Frameworks (MOFs) are still poorly investigated and understood. Bovine serum albumin (BSA), used as a model protein, was immobilized within two different zeolitic imidazolate frameworks (ZIF-zni and ZIF-8). Pristine ZIFs and BSA@ZIFs were characterized by X-ray diffraction, small-angle X-ray scattering, scanning electron microscopy, confocal laser scanning microscopy, thermogravimetric analysis, micro-FTIR and confocal Raman spectroscopy to characterize MOFs structure and the protein location in the materials. Moreover, the secondary structure and conformation changes of BSA after immobilization on both ZIFs were studied with FTIR. BSA is located both in the inner and on the outer surface of MOFs, forming domains that span from the micro- to the nanoscale. BSA crystallinity (β-sheets + α-helices) increases up to 25% and 40% for ZIF-zni and ZIF-8, respectively with a consequent reduction of β-turns due to immobilization within MOFs.

Keywords: Zeolitic imidazolate Frameworks (ZIFs) • BSA • Immobilization • Protein location and conformation • Biomimetic mineralization

Introduction

Metal Organic Frameworks (MOFs) are porous hybrid materials constituted by a metal node and an organic ligand linked through coordination bonds.[1] The first publication about MOFs dates back to 1989,[2] but the term MOF was first used by Yaghi in 1995.[3] Since then, the interest for these materials has steadily increased and numerous MOFs have been synthesized.[2,4–6] Due to their proprieties, such as high porosity (up to 90% free volume) and surface area (extending beyond 6000 m^2 g^{-1}),[7] MOFs have been explored for several applications, like removal of water pollutants,[8] gas adsorption,[9] catalysis,[10] sensing, drug delivery,[11] etc.[8,12] Recently, MOFs have shown great potential as enzyme immobilization supports.[13] The main advantages of immobilized versus free enzymes involve their higher stability to environmental changes (pH, temperature, etc.), the possibility to be easily separated from the reaction mixture and reused, and also their possible use in continuous processes.[14,15] Compared to the other immobilization methods, enzyme immobilization on MOFs, obtained through either chemical (covalent attachment and cross linking) or physical methods (entrapment and adsorption),[16] is especially advantageous as it allows the rapid and facile preparation of heterogeneous biocatalysts under mild conditions (in aqueous solution, moderate pH, atmospheric pressure and at room temperature) using low cost and commercially available starting materials.[13,15,17–20] Recent research on enzyme immobilization on MOFs has focused on zeolitic imidazolate frameworks (ZIFs), which are crystalline solids consisting of either Zn^{2+} or Co^{2+} metal ions and organic imidazolate ligands with topologies based on those of tetrahedral zeolites.[21] Lyu et al. firstly immobilized cytochrome c on a ZIF obtaining a substantial increase of catalytic activity in comparison with the free enzyme.[22] Since then, different approaches were used to find the optimal immobilization method which allowed to retain a high enzymatic activity and stability.[16] Among them, the encapsulation method has proven to be faster and cheaper than other methodologies, leading to suitable biocatalysts for industrial processes,[23] with both high catalytic activity and thermal stability.[24] For instance, Falcaro et al. encapsulated an urease in ZIF-8 finding an increase in thermal stability compared to the free enzyme.[25] In the context of enzymatic biodiesel

production, Rafiei et al. reported the encapsulation of *Candida rugosa* lipase into ZIF-67,[26] while Adnan et al. encapsulated the lipase from *Rhizomucor miehei* within X-shaped ZIF-8.[27] Knedel et al. investigated the stability and selectivity at various temperatures and different organic solvents of the CgL1 laccase from *Corynebacterium glutamicum* encapsulated within ZIF-8.[28] Wu et al. prepared an immobilized multiple-enzyme system within ZIF-8 which was used as a colorimetric sensor for glucose detection.[29]

Despite these advances, two crucial open issues involve: i. the location (either in the inner or outer support surface) of the enzyme encapsulated within the MOF,[15,30–32] and ii. the quantification of the enzyme structure distortion due to its interaction with the MOF support. The former has been so far mainly addressed by labelling enzymes with fluorescein isothiocyanate (FITC), a marker which reacts with surface amino groups of most proteins,[33] allowing for enzyme detection by confocal laser scanning microscopy (CLSM).[34] Other methods have also been reported,[35] including the analysis of the enzyme@MOF morphology pre- and post-calcination by scanning electron microscopy (SEM).[34] The latter has been mainly addressed using spectroscopic techniques such as UV-Vis, FT/IR, Raman, and circular dichroism. Since commercial enzymes often show a very low grade of purity, the investigation of their conformation due to the immobilization is tricky and poorly investigated.[36] Aiming to address these two open and challenging topics, we investigated here the location of the model protein bovine serum albumin (BSA) immobilized within two zeolitic imidazolate frameworks, namely, ZIF-zni and ZIF-8. These materials are crystalline MOFs both consisting of Zn^{2+} metal ions with different ligands, that is 1H-imidazole and 2-methyl-1H-imidazole for ZIF-zni and ZIF-8, respectively. To this purpose, ZIF-zni, ZIF-8, BSA@ZIF-zni and BSA@ZIF-8 samples were characterized using an extensive analytical setup able to achieve complementary structural information. XRD (X-ray diffraction) was used to analyze the crystallinity of the samples. Their structures at the nanoscale were investigated through small angle X-ray scattering (SAXS). SEM and CLSM were employed to evaluate the morphological properties of the samples and to investigate the protein location at the microscale. Chemical composition was determined through

thermogravimetric analysis (TGA), whilst the spectroscopic characterization of BSA, ZIFs, and BSA@ZIFs samples was performed by attenuated total reflection Fourier transform infrared spectroscopy (ATR-FTIR), micro-FTIR and confocal Raman spectroscopy. In particular, micro-FTIR 2D imaging using a Focal Plane Array (FPA) detector was used to investigate the secondary structure and conformation changes of BSA upon its immobilization on ZIF-zni (BSA@ZIF-zni) and ZIF-8 (BSA@ZIF-8).

Results and Discussion

ZIF-zni, ZIF-8, BSA BSA@ZIF-zni, and BSA@ZIF-8 samples were characterized through XRD. The XRD patterns confirm the formation of the ZIF-zni (Figure 1A) and ZIF-8 (Figure 1B) materials, with characteristic peaks at 15°, 17°, 18°, 21° and at 7.4°, 10.5°, 12.8°, 14.8°, respectively.[20,37] The XRD patterns obtained for BSA@ZIF-zni and BSA@ZIF-8 samples are equal to those of the pure ZIFs, demonstrating that BSA does not meaningfully alter the structure of the MOFs.

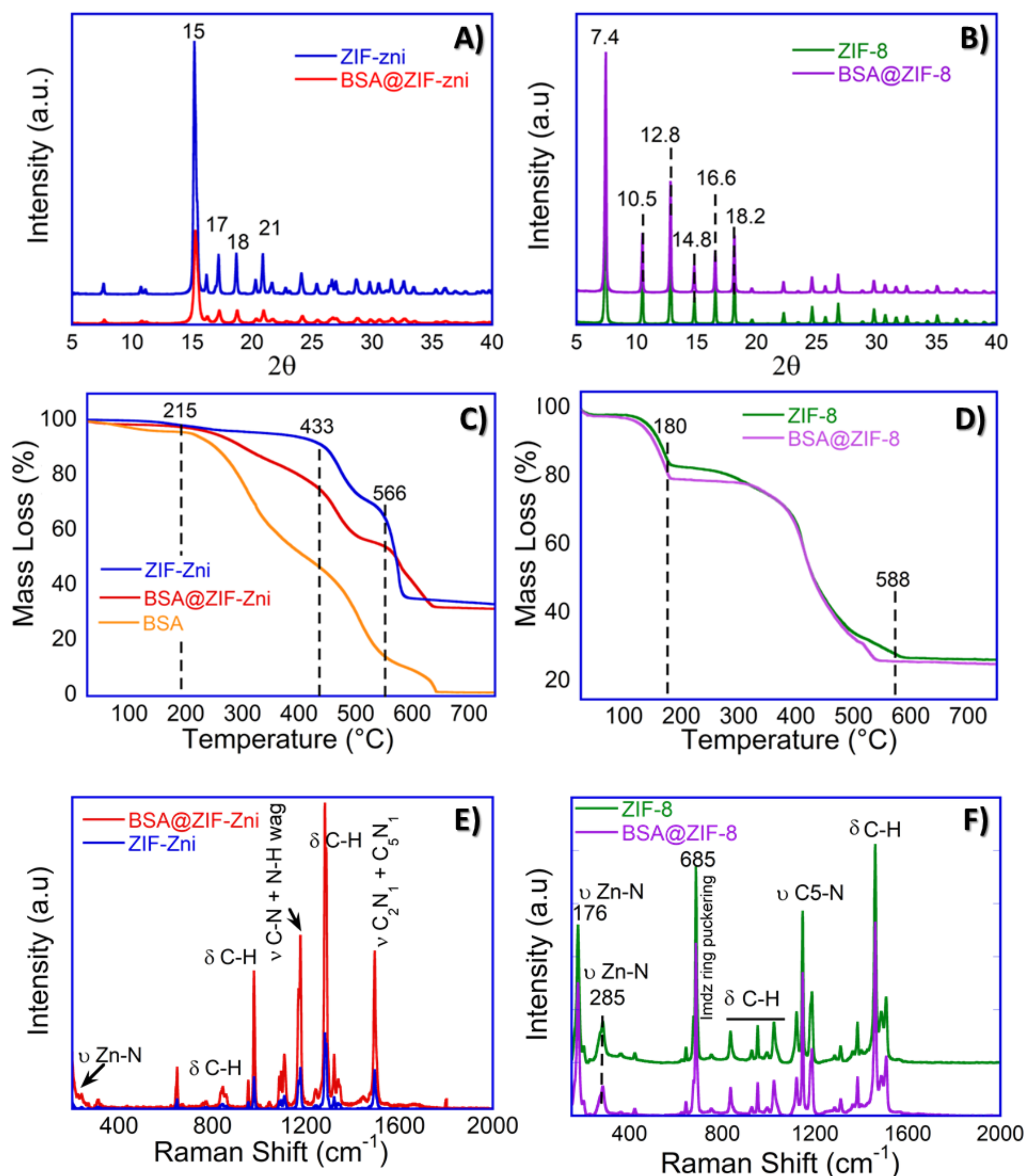

Figure 1. Samples characterization: XRD patterns of **A)** ZIF-zni and BSA@ZIF-zni; **B)** ZIF-8 and BSA@ZIF-8. Thermogravimetric analysis (TGA) curves from 25 °C to 800 °C of: **C)** ZIF-zni. BSA@ZIF-zni and BSA and **D)** ZIF-8 and BSA@ZIF-8. Raman spectrum of **E)** ZIF-zni, BSA@ZIF-zni and **F)** ZIF-8, BSA@ ZIF-8 (wavenumber range from 150 to 2000 cm^{-1}).

Pristine materials and BSA@ZIFs were characterized by TGA (Fig.2A). Both ZIF-zni and BSA@ZIF-zni samples show a slight mass decrease (~2.7%) between 25 and 215 °C due to humidity loss. ZIF-zni exhibited good thermal stability in air, up to 433 °C, in agreement with the literature.[13] ZIF-zni had mass losses of 37.7 % and 26.0 % over the ranges, 433 – 566 °C and 566 – 800 °C,

respectively. The first mass loss can be attributed to the partial loss of ZIF crystallinity which is favored in oxidizing environments, while the latter can be ascribed to the complete decomposition and collapse of the ZIF-zni structure. TGA of BSA@ZIF-zni was comparable with ZIF-zni except for the mass loss of 21 % over the temperature range, 215 –433°C assigned to the encapsulated protein molecules (Table S1; Supporting information file). ZIF-8 and BSA@ZIF-8 are stable up to 100 °C. Both materials displayed a similar mass loss of approximately ~ 20% in the temperature range 100 – 180 °C ascribable to the removal of water and unreacted reagents. ZIF-8 and BSA@ZIF-8 showed a mass loss of ~ 6 % and ~ 10 % over the range 180 –360 °C, respectively. This is associated to the thermal decomposition of BSA molecules encapsulated within the ZIF-8. The mass loss at temperatures higher than 360°C is likely due to the decomposition of the ZIF-8 structure.

The Raman spectra of ZIF-zni, BSA@ZIF-zni, ZIF-8 and BSA@ZIF-8 samples are shown in Figures 1E and 1F.[38–40] The ZIF-zni spectrum showed a shift of ν Zn-N toward lower cm^{-1} compared to ZIF-8. ZIF 8 showed intense bands at 176 cm^{-1}, 685 cm^{-1}, 1146 cm^{-1}, and 1458 cm^{-1} ascribable to Zn−N stretching, imidazole ring puckering, C5−N stretching and methyl bending, respectively (Figure 1F). The Raman spectra obtained for BSA@ZIF-zni and BSA@ZIF-8 samples do not present substantial differences from those of pristine ZIF materials demonstrating that the inclusion of BSA does not alter chemical functions in the MOFs. The ZIF-zni and ZIF-8 textural properties like surface area and pore volume were characterized through nitrogen adsorption−desorption isotherms. ZIF-zni network topology is the densest of all known ZIF structures and is essentially non-porous.[41,42] Results regarding ZIF-zni show a non-porous material agreeing with what was reported in the literature (Table S1, see SI).[43] The network topology of ZIF-8 (sodalite, SOD topology) is less dense compared with that of ZIF-zni (zni topology). Data results confirm the type-I isotherm typical for ZIF-8 microporous materials (see Table S1, Figure S1). ZIF-8 had a S_{BET} of 1760 m^2 g^{-1} that decreased by 7% (1640 m^2 g^{-1}) in the presence of BSA (BSA@ZIF-8). Similarly, pore volume (V_p) decreased from 0.625 cm^3 g^{-1} (ZIF-8) to 0.582 cm^3 g^{-1} for BSA@ZIF-8. The encapsulation

efficiencies (EE) of BSA into the MOFs were 98% and 82% for BSA@ZIF-zni and BSA@ZIF-8 respectively (see Table S1).

Scanning electron microscopy (SEM) images (Figure 2) of ZIF-zni show a regular morphology with a rod shape similar to that of ZIF-7.[44] BSA immobilization into ZIF-zni resulted in a change of morphology from rod shapes to spherical particles.[13,45] SEM characterization of ZIF-8 clearly shows the expected rhombic dodecahedron geometry typical of ZIF-8 in SOD phase.[46] The same morphology was obtained for BSA@ZIF-8 according with previous works.[47] Liang et al. immobilized different enzymes into ZIF-8, showing that the morphology of enzyme@ZIF-8 particles changed depending on the type of immobilized biomacromolecules. Indeed, typical rhombic ZIF-8 dodecahedron crystal morphology was observed for immobilized ribonuclease A, lipase, urease, and lysozyme, whereas for immobilized ovalbumin, horseradish peroxidase, and trypsin leaves, flowers, and stars morphologies were obtained, respectively.[48]

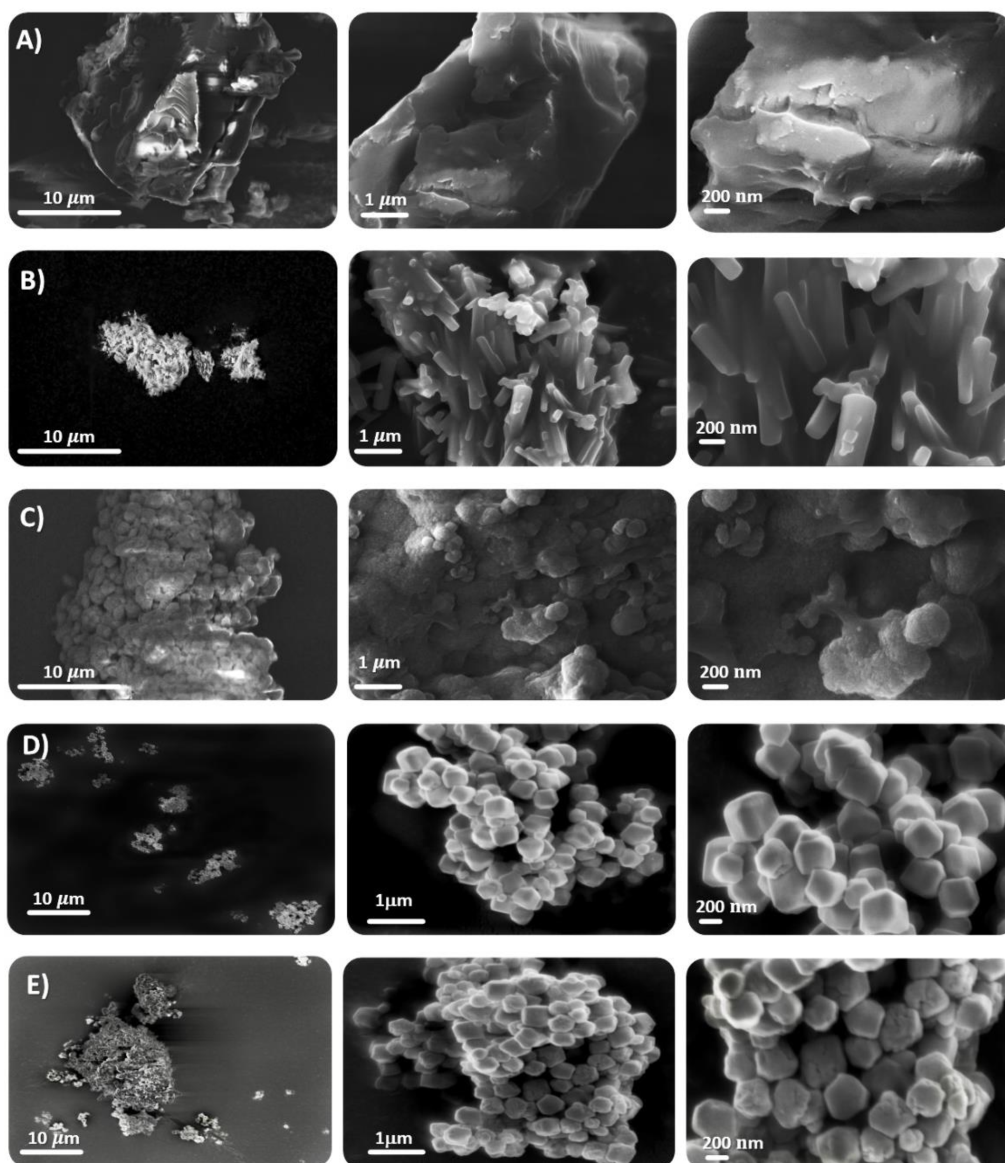

Figure 2. SEM images of **A**) BSA, **B**) ZIF-zni, **C**) BSA@ZIF-zni, **D**) BSA@ ZIF-8, and **E)** ZIF-8.

In order to investigate the location of the immobilized BSA protein, SEM images were acquired after sample calcination at 360 °C for 2 hours (Figure 3A and Figure 3B). The calcination temperature was chosen based on the thermal gravimetric analysis (Figure 1C and 1D). Due to the calcination, a change of the morphology from spherical and rhombic dodecahedron shape to pitted and uneven particles was observed for BSA@ZIF-zni and BSA@ZIF-8, respectively. This is likely ascribable to the presence of BSA within ZIFs frameworks, which because of the combustion leads to rifts in the materials.

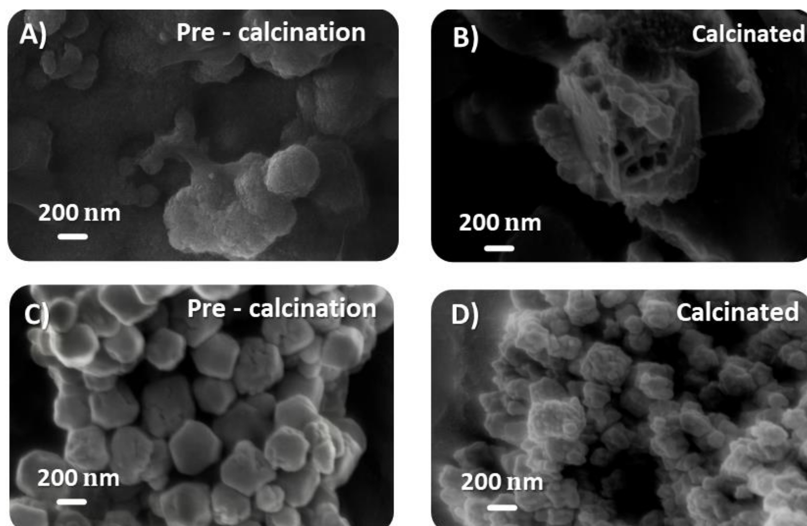

Figure 3. SEM images of **A)** BSA@ZIF-zni **B)** BSA@ZIF-zni post calcination at 360 °C **C)** BSA@ZIF-8 **D)** BSA@ZIF-8 post calcination at 360 °C.

Further insights on MOFs structure at the nanoscale were gained through small/wide angle X-ray scattering (SWAXS) analysis. More specifically, the effects of BSA loading, and successive removal by calcination, were investigated. SWAXS profiles of the ZIFs, BSA@ZIFs and calcinated BSA@ZIFs are shown in Figures 6A and 6B. The comparison among the curves suggests that BSA loading induces the formation of nanoscale inhomogeneities.[48,49] The calcinated MOFs profiles show that nanoscale features are still present after the protein removal. SAXS curves were fitted according to a model consisting in a Porod contribution (A/Q^n at low Q) and a Guinier-Porod term, in agreement with the literature for similar systems.[48,50] The Guinier-Porod term describes the gyration radius of scattering objects, R_g, with dimensionality parameter, s (s = 0 for spheres, 1 for rods and 2 for platelet objects) and a Porod slope at high-Q, m. The complete analytical details on the model are reported in the Experimental section (i.e. supporting information file) while fitting parameters are listed in Table 1.

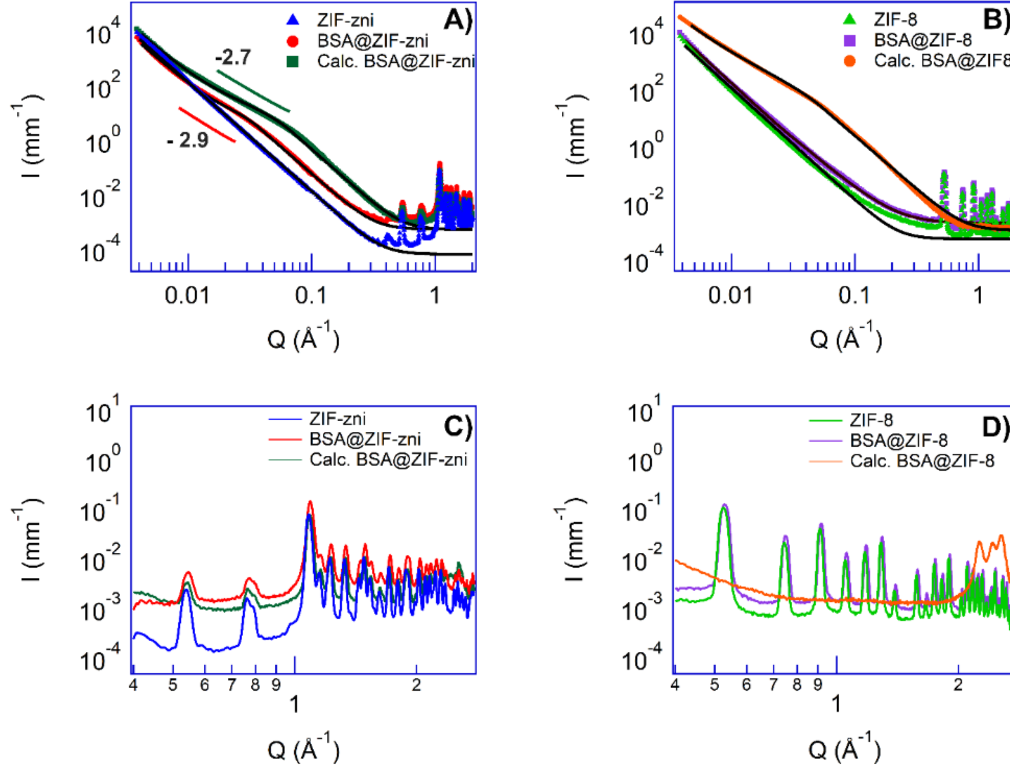

Figure 4. SAXS profile of the investigated MOFs. **A)** ZIF-zni (blue triangles), BSA@ZIF-zni (red circles) and calcinated BSA@ZIF-zni (dark green squares); the slopes indicate the mass fractal dimensions of BSA@ZIF-zni (red) and calcinated BSA@ZIF-zni (green); **B)** ZIF-8 (light green triangles), BSA@ZIF-8 (purple squares) and calcinated BSA@ZIF-8 (orange circles). Bottom panel: details of the WAXS region for ZIF-zni **(C)** and ZIF-8 **(D)** MOFs.

Table 1. SAXS fitting parameters of MOFs, BSA@MOFs and calcinated BSA@MOFs.

Samples	A (Scale), $\times 10^{-6}$	n (Porod low-Q)	B (Scale)	R_g (nm)	s	m (Porod high-Q)	Bkg$\times 10^{-3}$
ZIF-zni	1.62 ± 0.01	4.00 ± 0.05	-	-	-	-	0.07 ± 0.01
BSA@ZIF-zni	2.00 ± 0.01	3.86 ± 0.05	5.63 ± 0.01	6.0 ± 0.1	0.26 ± 0.01	4.00 ± 0.05	0.5 ± 0.1
Calc. BSA@ZIF-zni	1.99 ± 0.01	4.00 ± 0.05	0.036 ± 0.001	1.4 ± 0.1	1.78 ± 0.01	4.00 ± 0.05	0.5 ± 0.1
ZIF-8	1.35 ± 0.01	3.94 ± 0.05	-	-	-	-	1.1 ± 0.1
BSA@ZIF-8	1.50 ± 0.01	4.00 ± 0.05	0.511 ± 0.001	4.3 ± 0.1	0.00 ± 0.01	2.66 ± 0.05	1.8 ± 0.1
Calc. BSA@ZIF-8	17.90 ± 0.01	3.76 ± 0.05	0.144 ± 0.001	1.7 ± 0.1	1.98 ± 0.01	3.75 ± 0.01	1.0 ± 0.1

The SAXS fitting parameters suggest that at large length scales (i.e., low Q) the samples are characterized by a smooth surface ($n \approx 4$). Pure ZIF-8 and ZIF-zni curves do not show other significant features. In BSA@ZIFs curves, a knee at about 0.1 Å^{-1} arises, which can be associated to objects with gyration radius $R_g = 6.0 \pm 0.1$ nm (BSA@ZIF-zni) and 4.3 ± 0.1 nm (BSA@ZIF-8). More specifically, it describes the mesopores in which BSA is located. According to previous

findings,[48,49] such pore size in BSA@ZIF-8 can accommodate monomeric BSA. The parameter *s* is associated to spherical pores for BSA@ZIF-8, and slightly elliptical pores in the case of BSA@ZIF-zni. After calcination, pores significantly shrink and become platelet-like ($s \approx 2$), that is, protein removal likely causes the formation of cracks inside the MOF structure. No alterations were found in ZIF-zni structure due to calcination (Figure 4 C) whilst the crystalline structure of ZIF-8 is evidently changed (Figure 4 D). ZIF-8 structure alteration at high temperature was described by Joshua et al.[51] The formation of sub-micron porosity in ZIF-8 after calcination, observed through SEM, is usually ascribed to surficial proteins/enzymes removal.[34,52] In these cases, the material morphology is claimed to be not damaged by the heating process. SEM images collected here (Figure 5B) confirm that the morphology of the material is not significantly altered by calcination. Nonetheless, fitting parameters (R_g, *s, m*, and *n*) of calcinated BSA@ZIF-8 should be considered with caution. A variation of the mass fractal dimension is evident in BSA@ZIF-zni, after calcination, that is the slope of the Guinier region changes from -2.9 to -2.7 (Figure 4A). This indicates a slight reduction of the objects' compactness (lower clustering) and is related to the protein removal. Finally, it is worth noting that the B scale parameter, related to scattering in the 0.01-0.3 $Å^{-1}$ region, is one or two orders of magnitude higher for BSA@ZIF-zni than for the other samples. As protein loading does not strongly differ, being 163 mg g^{-1} for BSA@ZIF-zni and 140 mg g^{-1} for BSA@ZIF-8 (Table S1), this could be related to a higher BSA accumulation on ZIF-zni outer surface, as observed in SEM micrographs.

Confocal microscope images of FITC-BSA@ZIF-zni and FITC-BSA@ZIF-8 samples (Figure 7) show homogeneous distribution of BSA molecules within the MOFs. This result suggests that BSA could be both encapsulated within ZIFs structure and on the external surface of the material, especially in ZIF-zni, where high fluorescence intensity areas can be identified more easily with surficial protein.[24]

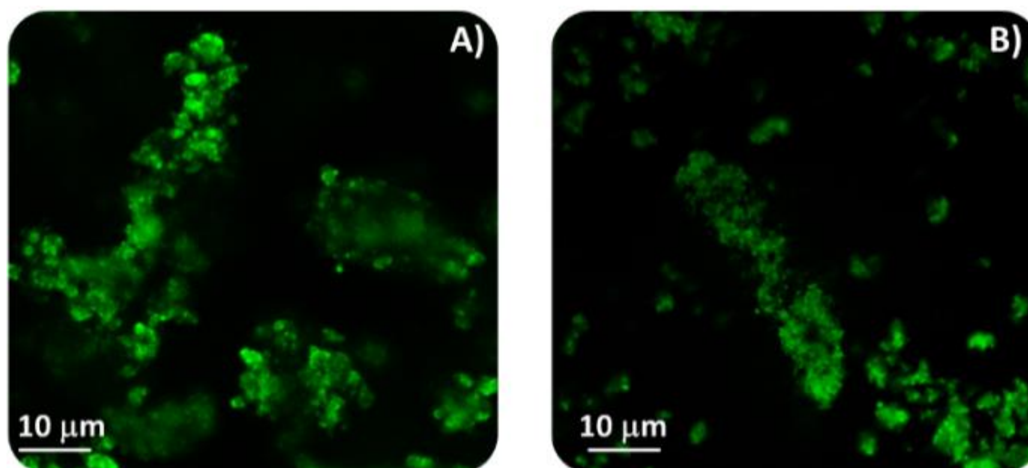

Figure 5. Confocal laser A) BSA-FITC@ZIF-zni and B) BSA-FITC@ZIF-8 samples.

FTIR 2D Imaging provided further information on the location and on the state of protein in the BSA@ZIF-zni sample. Mapping the absorbance intensity (peak area) of the 3450-3200 cm^{-1} and 1565-1525 cm^{-1} regions, which correspond respectively to the central portion of amide A and to the amide II band of BSA, showed that the protein is found all over the MOF in BSA@ZIF-zni (Figure S2). In addition, details of the imaging maps at higher magnification (see Figure S4) highlighted that the protein seems to concentrate in domains of 5-40 μm, which form an extended network across the MOF surface, while such domains are not observed in the pure BSA sample. Imaging of amide A and amide II was preferred to amide I, to avoid interferences from absorptions of ZIF-zni in the 1720-1600 cm^{-1} region, ascribed to overtone and combination bands of imidazole.[53] Distribution of the protein in micro-domains was also observable in BSA@ZIF-8 (Figures S3 and S5), even though not as evident as in BSA@ZIF-zni. Simply looking at the IR reflectance spectra, it is also possible to observe that the amide II band in BSA@ZIF-zni has a clear redshift of ca. 25 cm^{-1} compared to pure BSA (Figure S6). A similar red shift seems to occur also to amide I, even though its determination is less clear owing to modifications of the band in BSA@ZIF-zni and its overlap with ZIF-zni absorptions in the same region. Amide I derives mainly from C=O and C-N stretching vibrations, while amide II from N-H bending with some C-N and C-C stretching contribution; a redshift indicates

bond elongation of these functional groups, which points to the formation of interactions between the protein and the MOF structure.

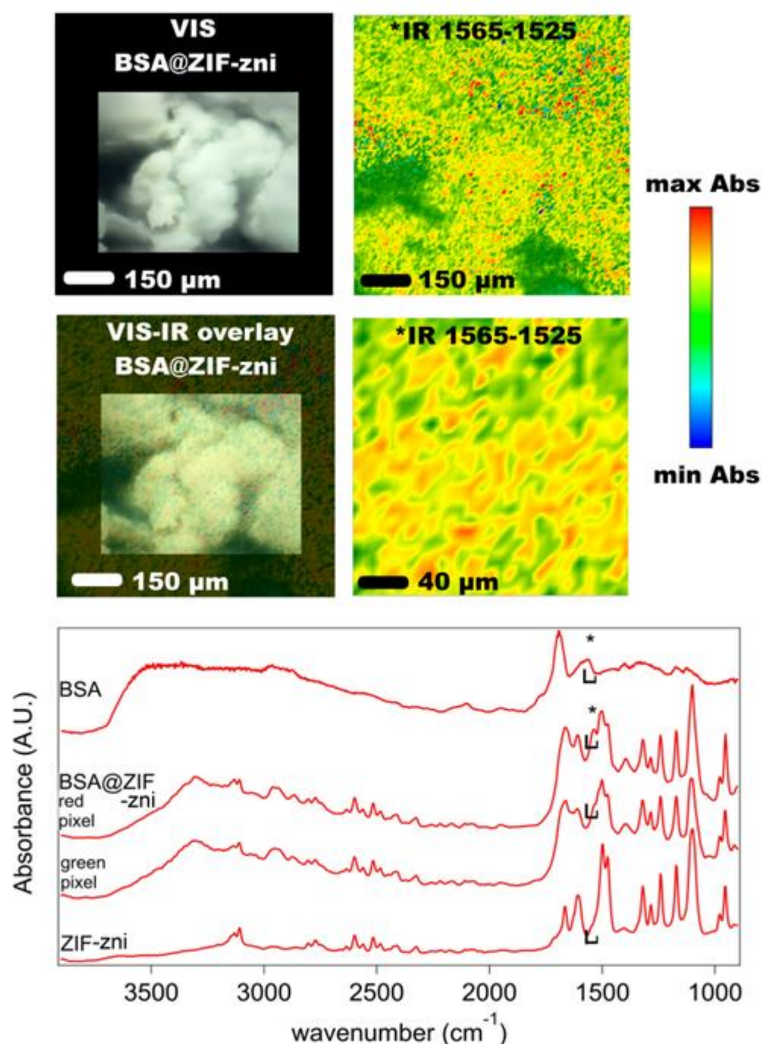

Figure 6. (Top panel, upper row) Visible (VIS) and FTIR 2D Imaging maps of the BSA@ZIF-zni sample. The IR maps were obtained imaging the absorbance intensity (peak area) of the amide II band of BSA in the 1565-1525 cm^{-1} region. (Top panel, lower row) Overlay of the VIS and IR maps, and detail of the IR map highlighting the micrometric domains where the amide II band is more intense (red pixels). (Lower panel) Reflectance spectra of ZIF, BSA and BSA@ZIF-zni samples. The BSA and ZIF-zni spectra were obtained on the pure BSA and ZIF-zni samples, respectively, and are showed as references. The spectra of BSA@ZIF-zni relate each to one pixel (5.5 x 5.5 μm^2) of the IR maps of the top panel; two spectra are showed representative of, respectively, red, and green pixels in the maps. The "*" and brackets highlight the amide II band and the spectral region that was imaged in the maps

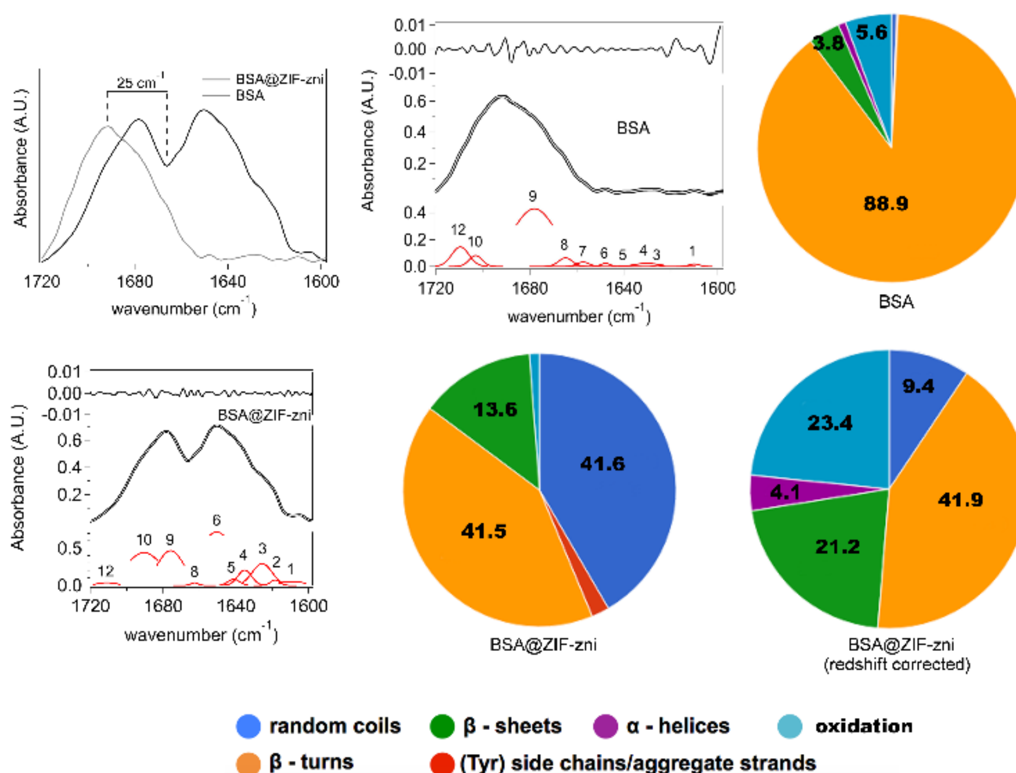

Figure 7. (Top left) FTIR Reflectance spectra of BSA and BSA@ZIF-zni (after subtraction of a representative ZIF-zni spectrum) in the 1720-1600 cm^{-1} region (amide I). The 25 cm^{-1} redshift in the BSA@ZIF-zni spectrum was evaluated comparing the regions of amide I and II (see also Figure S6) with those of BSA. (Top center, bottom left) Spectral deconvolution of the BSA and BSA@ZIF-zni amide I bands. The bands' components are numbered as in Section 3.5 (supporting information), without considering the redshift for BSA@ZIF-zni; the y-axis reports the absorbance of the components (red bands), the experimental spectrum (thick black line), the fitting curve (thin white line inside the experimental curve), and the fitting residuals (black line on top of the spectra). (Top right, bottom right and center) The average secondary structure for BSA and BSA@ZIF-zni is reported in the pie charts, grouping the main structure types (relative error is ca. 0.05). For BSA@ZIF-zni, the structure composition was also recalculated considering the 25 cm^{-1} redshift of the amide I components, considering the original component 12 as a baseline band.

Additional information on changes in the BSA structure upon immobilization was extracted by the deconvolution of the amide I band in the reflectance spectra. Figure 7 shows a comparison between the amide I band of BSA and that of BSA@ZIF after subtraction of the ZIF absorptions. Besides the aforementioned redshift, the band of the immobilized protein has a completely different shape with two maxima, a clear hint that structural modification has occurred. Before interaction with the MOF, amide I deconvolution indicates that BSA has a strong content in β-turns (~89%), with limited contribution from β-sheets (~4%). This is in contrast with studies in the literature where BSA structure, obtained from circular dichroism and calculations on the mean residual ellipticity, was

found to be strongly based on α-helices (67%) with contributions from β-turns and extended chains (10% and 23% respectively).[54] However, Lu et al. found, using ATR-FTIR and spectral deconvolution, a significantly lower α-helices content and larger contributions from β-turns and random coils;[55] considering also that contact pressure in ATR experiments can cause orientation of protein domains and an overestimation of crystalline phases,[56,57] these findings are in less sharp contrast with the results reported here. Indeed, we found much closer values to Lu et al. when we analyzed BSA in ATR, rather than reflectance mode (Figure S8). Another possible explanation is that, in principle, a partially derivative shape of the amide I band in the reflectance spectra might result in some overestimation of β-turns over α-helices, even though in our case amide I band distortion in the reflectance spectra of BSA did not seem to occur to a large extent (see Figure S2 and Figure S3). Most importantly to the purposes of this study, the crystalline content of BSA increases significantly when the protein is immobilized on the MOF in BSA@ZIF-zni (Figure 7). This is true even before correcting the wavenumbers of the amide I components to the 25 cm^{-1} red-shift, and becomes more evident after correction, with a crystalline content increase up to ~25% (β-sheets + α-helices), and a drastic reduction of β-turns. Some increase in random coils occurred too, which accounts also for the formation of extended chains. Finally, the increase of oxidation bands can be ascribed to treatment with zinc nitrate (an oxidant) during the protein immobilization steps. A significant increase in the crystalline content of BSA@ZIF-zni and BSA@ZIF-8 was observed also when the samples were analyzed with ATR (Figure S8 and Figure S9), which overall corroborates our conclusion that BSA structure is ordered through immobilization on the MOF. In the case of BSA@ZIF-zni, the amide I band in the ATR spectra shows a marked redshift (ca. 50 cm^{-1}) from the protein's band before immobilization, i.e. even larger than in the reflectance spectra of the same sample. A marked red shift of amide I, indicating protein-MOF interactions, and protein structuration, was also observed on BSA@ZIF-8 (see Figure 8 and Figure S7). Interestingly, a more pronounced

ordering of the protein by the MOF is observed than in BSA@ZIF-zni. In addition, oxidation bands were in this case almost absent.

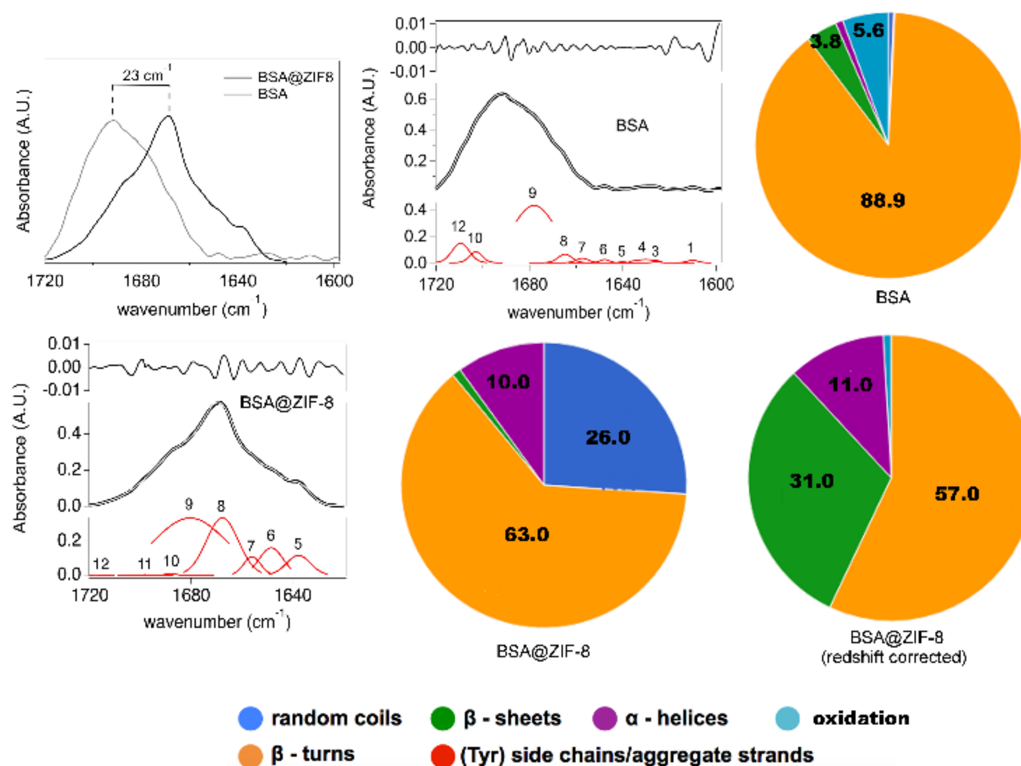

Figure 8. (Top left) FTIR Reflectance spectra of BSA and BSA@ZIF-8 (after subtraction of a representative ZIF-8 spectrum) in the 1720-1600 cm-1 region (amide I). The 23 cm^{-1} redshift in the BSA@ZIF-8 amide I is also evident before subtraction of the ZIF-8 absorptions (see Figure S7). (Top center, bottom left) Spectral deconvolution of the BSA and BSA@ZIF-8 amide I bands. The bands' components are numbered as in Section 3.5, without considering the redshift for BSA@ZIF8; the y-axis reports the absorbance of the components (red bands), the experimental spectrum (thick black line), the fitting curve (thin white line inside the experimental curve), and the fitting residuals (black line on top of the spectra). (Top right, bottom right and center) The average secondary structure for BSA and BSA@ZIF-8 is reported in the pie charts, grouping the main structure types (relative error is ca. 0.05). For BSA@ZIF-8, the structure composition was also recalculated considering the 23 cm^{-1} redshift of the amide I components, considering the original component 12 as a baseline band.

Conclusions

Among the enzyme immobilization methods reported in the literature, the enzymatic encapsulation received immense attention in these last years due to its rapid and mild condition procedure. Although the location of the enzyme (within/onto) in the material has already been investigated through confocal laser scanning microscope (CLSM) and TGA coupled with SEM, these techniques do not

precisely determine enzyme location, making necessary the combination of different methods to evaluate the protein location. Here, we investigated the location of the model protein bovine serum albumin (BSA) during its in-situ immobilization within two different zeolitic imidazolate frameworks (ZIF-8 and ZIF-zni). Data collected by CLSM and micro-FTIR showed that BSA is evenly distributed in domains of 5-40 μm around the material particles. SAXS analysis, performed on BSA@MOFs pre- and post-calcination, confirmed the BSA immobilization within both ZIF-8 and ZIF-zni, more specifically in inhomogeneities of ca. 4 and 6 nm, respectively. Moreover, higher scattering intensity from ZIF-zni could be related to an excess of protein accumulation on the outer surface of the MOF. This would confirm that BSA lies both inside ZIF-zni matrix and on its outer surface. Moreover, the quantification of enzyme structure distortion due to its interaction with MOF support is poorly investigated. FTIR deconvolution data showed that the crystalline content of BSA increases upon immobilization on the MOFs: free BSA has a strong content in β-turns (~ 89%), with limited contribution from β-sheets (~4%), whilst the crystalline content of BSA increases significantly when the protein is immobilized on both ZIF-zni and ZIF-8, resulting in increased up to ~ 25% (β -sheets + α -helices), and 40 % (β-sheets + α-helices), respectively, and a consequent drastic reduction of β-turns. Undoubtedly, this work has shed some light on some crucial points such as the protein location and its secondary structure change due to the immobilization on two different imidazolate-based frameworks and will stimulate further research on enzymes@MOFs.

Acknowledgements

AS acknowledges financial supports from Fondazione di Sardegna (FdS, F72F20000230007) and Regione Autonoma della Sardegna L.R.7 (CRP:RASSR79857). DT thanks MIUR (PON RI 2014-2020, Azione “l.1 "Dottorati Innovativi con Caratterizzazione industriale"- DOT1304455 2) for financing his PhD scholarship. All authors kindly acknowledge partial financial support from the

Italian Center for Colloid and Surface Science, CSGI. The authors are grateful to Dr. Rita Gelli (University of Florence, Italy) for the Raman spectra acquisition.

References

[1] S.R. Batten, N.R. Champness, X.-M. Chen, J. Garcia-Martinez, S. Kitagawa, L. Öhrström, M. O'Keeffe, M. Paik Suh, J. Reedijk, Terminology of metal–organic frameworks and coordination polymers (IUPAC Recommendations 2013), Pure Appl. Chem. 85 (2013) 1715–1724. https://doi.org/10.1351/PAC-REC-12-11-20.

[2] B.F. Hoskins, R. Robson, Infinite polymeric frameworks consisting of three dimensionally linked rod-like segments, J. Am. Chem. Soc. 111 (1989) 5962–5964. https://doi.org/10.1021/ja00197a079.

[3] O.M. Yaghi, H. Li, Hydrothermal Synthesis of a Metal-Organic Framework Containing Large Rectangular Channels, J. Am. Chem. Soc. 117 (1995) 10401–10402. https://doi.org/10.1021/ja00146a033.

[4] A.R. Millward, O.M. Yaghi, Metal−Organic Frameworks with Exceptionally High Capacity for Storage of Carbon Dioxide at Room Temperature, J. Am. Chem. Soc. 127 (2005) 17998–17999. https://doi.org/10.1021/ja0570032.

[5] Y. Yang, X. Arqué, T. Patiño, V. Guillerm, P.-R. Blersch, J. Pérez-Carvajal, I. Imaz, D. Maspoch, S. Sánchez, Enzyme-Powered Porous Micromotors Built from a Hierarchical Micro- and Mesoporous UiO-Type Metal–Organic Framework, J. Am. Chem. Soc. 142 (2020) 20962–20967. https://doi.org/10.1021/jacs.0c11061.

[6] M. Sanchez-Sanchez, I. de Asua, D. Ruano, K. Diaz, Direct Synthesis, Structural Features,

and Enhanced Catalytic Activity of the Basolite F300-like Semiamorphous Fe-BTC Framework, Cryst. Growth Des. 15 (2015) 4498–4506. https://doi.org/10.1021/acs.cgd.5b00755.

[7] H. Furukawa, N. Ko, Y.B. Go, N. Aratani, S.B. Choi, E. Choi, A.Ö. Yazaydin, R.Q. Snurr, M. O'Keeffe, J. Kim, O.M. Yaghi, Ultrahigh Porosity in Metal-Organic Frameworks, Science (80-.). 329 (2010) 424–428. https://doi.org/10.1126/science.1192160.

[8] G.R. Delpiano, D. Tocco, L. Medda, E. Magner, A. Salis, Adsorption of Malachite Green and Alizarin Red S Dyes Using Fe-BTC Metal Organic Framework as Adsorbent, Int. J. Mol. Sci. 22 (2021) 788. https://doi.org/10.3390/ijms22020788.

[9] G. Autie-Castro, M.A. Autie, E. Rodríguez-Castellón, C. Aguirre, E. Reguera, Cu-BTC and Fe-BTC metal-organic frameworks: Role of the materials structural features on their performance for volatile hydrocarbons separation, Colloids Surfaces A Physicochem. Eng. Asp. 481 (2015) 351–357. https://doi.org/10.1016/j.colsurfa.2015.05.044.

[10] K. Hemmer, M. Cokoja, R.A. Fischer, Exploitation of Intrinsic Confinement Effects of MOFs in Catalysis, ChemCatChem. 13 (2021) 1683–1691. https://doi.org/10.1002/cctc.202001606.

[11] M.-X. Wu, Y.-W. Yang, Metal-Organic Framework (MOF)-Based Drug/Cargo Delivery and Cancer Therapy, Adv. Mater. 29 (2017) 1606134. https://doi.org/10.1002/adma.201606134.

[12] D. Tocco, C. Carucci, M. Monduzzi, A. Salis, E. Sanjust, Recent Developments in the Delignification and Exploitation of Grass Lignocellulosic Biomass, ACS Sustain. Chem. Eng. 9 (n.d.) 2412–2432. https://doi.org/10.1021/acssuschemeng.0c07266.

[13] D. Tocco, C. Carucci, D. Todde, K. Shortall, F. Otero, E. Sanjust, E. Magner, A. Salis, Enzyme immobilization on metal organic frameworks: Laccase from Aspergillus sp. is better

adapted to ZIF-zni rather than Fe-BTC, Colloids Surfaces B Biointerfaces. 208 (2021) 112147. https://doi.org/10.1016/j.colsurfb.2021.112147.

[14] V. Gascón, M.B. Jiménez, R.M. Blanco, M. Sanchez-Sanchez, Semi-crystalline Fe-BTC MOF material as an efficient support for enzyme immobilization, Catal. Today. 304 (2018) 119–126. https://doi.org/10.1016/j.cattod.2017.10.022.

[15] V. Gascón, C. Carucci, M.B. Jiménez, R.M. Blanco, M. Sánchez-Sánchez, E. Magner, Rapid In Situ Immobilization of Enzymes in Metal–Organic Framework Supports under Mild Conditions, ChemCatChem. 9 (2017) 1182–1186. https://doi.org/10.1002/cctc.201601342.

[16] J. Boudrant, J.M. Woodley, R. Fernandez-Lafuente, Parameters necessary to define an immobilized enzyme preparation, Process Biochem. 90 (2020) 66–80. https://doi.org/10.1016/j.procbio.2019.11.026.

[17] P.D. Patil, G.D. Yadav, Rapid In Situ Encapsulation of Laccase into Metal-Organic Framework Support (ZIF-8) under Biocompatible Conditions, ChemistrySelect. 3 (2018) 4669–4675. https://doi.org/10.1002/slct.201702852.

[18] R.J. Drout, L. Robison, O.K. Farha, Catalytic applications of enzymes encapsulated in metal–organic frameworks, Coord. Chem. Rev. 381 (2019) 151–160. https://doi.org/10.1016/j.ccr.2018.11.009.

[19] M. Naseri, F. Pitzalis, C. Carucci, L. Medda, L. Fotouhi, E. Magner, A. Salis, Lipase and Laccase Encapsulated on Zeolite Imidazolate Framework: Enzyme Activity and Stability from Voltammetric Measurements, ChemCatChem. 10 (2018) 5425–5433. https://doi.org/10.1002/cctc.201801293.

[20] F. Pitzalis, C. Carucci, M. Naseri, L. Fotouhi, E. Magner, A. Salis, Lipase Encapsulation onto ZIF-8: A Comparison between Biocatalysts Obtained at Low and High Zinc/2-

Methylimidazole Molar Ratio in Aqueous Medium, ChemCatChem. 10 (2018) 1578–1585. https://doi.org/10.1002/cctc.201701984.

[21] F.J. Uribe-romo, C.B. Knobler, M.O. Keeffe, O.M. Yaghi, Capture Properties of Zeolitic Imidazolate Frameworks, Acc. Chem. Res. 43 (2010) 58–67.

[22] F. Lyu, Y. Zhang, R.N. Zare, J. Ge, Z. Liu, One-Pot Synthesis of Protein-Embedded Metal–Organic Frameworks with Enhanced Biological Activities, Nano Lett. 14 (2014) 5761–5765. https://doi.org/10.1021/nl5026419.

[23] R. Singh, M. Musameh, Y. Gao, B. Ozcelik, X. Mulet, C.M. Doherty, Stable MOF@enzyme composites for electrochemical biosensing devices, J. Mater. Chem. C. 9 (2021) 7677–7688. https://doi.org/10.1039/D1TC00407G.

[24] S.S. Nadar, V.K. Rathod, Encapsulation of lipase within metal-organic framework (MOF) with enhanced activity intensified under ultrasound, Enzyme Microb. Technol. 108 (2018) 11–20. https://doi.org/10.1016/j.enzmictec.2017.08.008.

[25] K. Liang, C.J. Coghlan, S.G. Bell, C. Doonan, P. Falcaro, Enzyme encapsulation in zeolitic imidazolate frameworks: a comparison between controlled co-precipitation and biomimetic mineralisation, Chem. Commun. 52 (2016) 473–476. https://doi.org/10.1039/C5CC07577G.

[26] S. Rafiei, S. Tangestaninejad, P. Horcajada, M. Moghadam, V. Mirkhani, I. Mohammadpoor-Baltork, R. Kardanpour, F. Zadehahmadi, Efficient biodiesel production using a lipase@ZIF-67 nanobioreactor, Chem. Eng. J. 334 (2018) 1233–1241. https://doi.org/10.1016/j.cej.2017.10.094.

[27] M. Adnan, K. Li, L. Xu, Y. Yan, X-Shaped ZIF-8 for Immobilization Rhizomucor miehei Lipase via Encapsulation and Its Application toward Biodiesel Production, Catalysts. 8 (2018) 96. https://doi.org/10.3390/catal8030096.

[28] T.O. Knedel, E. Ricklefs, C. Schlüsener, V.B. Urlacher, C. Janiak, Laccase Encapsulation in ZIF-8 Metal-Organic Framework Shows Stability Enhancement and Substrate Selectivity, ChemistryOpen. 8 (2019) 1337–1344. https://doi.org/10.1002/open.201900146.

[29] X. Wu, J. Ge, C. Yang, M. Hou, Z. Liu, Facile synthesis of multiple enzyme-containing metal–organic frameworks in a biomolecule-friendly environment, Chem. Commun. 51 (2015) 13408–13411. https://doi.org/10.1039/C5CC05136C.

[30] W.-H. Chen, M. Vázquez-González, A. Zoabi, R. Abu-Reziq, I. Willner, Biocatalytic cascades driven by enzymes encapsulated in metal–organic framework nanoparticles, Nat. Catal. 1 (2018) 689–695. https://doi.org/10.1038/s41929-018-0117-2.

[31] T.H. Wei, S.H. Wu, Y. Da Huang, W.S. Lo, B.P. Williams, S.Y. Chen, H.C. Yang, Y.S. Hsu, Z.Y. Lin, X.H. Chen, P.E. Kuo, L.Y. Chou, C.K. Tsung, F.K. Shieh, Rapid mechanochemical encapsulation of biocatalysts into robust metal–organic frameworks, Nat. Commun. 10 (2019) 1–8. https://doi.org/10.1038/s41467-019-12966-0.

[32] X. Li, D. Li, Y. Zhang, P. Lv, Q. Feng, Q. Wei, Encapsulation of enzyme by metal-organic framework for single-enzymatic biofuel cell-based self-powered biosensor, Nano Energy. 68 (2020) 104308. https://doi.org/10.1016/j.nanoen.2019.104308.

[33] C. Wang, K. Liao, Recent Advances in Emerging Metal– and Covalent–Organic Frameworks for Enzyme Encapsulation, ACS Appl. Mater. Interfaces. 13 (2021) 56752–56776. https://doi.org/10.1021/acsami.1c13408.

[34] M. Salgaonkar, S.S. Nadar, V.K. Rathod, Combi-metal organic framework (Combi-MOF) of α-amylase and glucoamylase for one pot starch hydrolysis, Int. J. Biol. Macromol. 113 (2018) 464–475. https://doi.org/10.1016/j.ijbiomac.2018.02.092.

[35] S.S. Nadar, L. Vaidya, V.K. Rathod, International Journal of Biological Macromolecules

Enzyme embedded metal organic framework (enzyme – MOF): De novo approaches for immobilization, Int. J. Biol. Macromol. 149 (2020) 861–876. https://doi.org/10.1016/j.ijbiomac.2020.01.240.

[36] F. Secundo, Conformational changes of enzymes upon immobilisation, Chem. Soc. Rev. 42 (2013) 6250. https://doi.org/10.1039/c3cs35495d.

[37] C. Zhou, M. Stepniewska, J.M. Sørensen, L. Scarpa, G. Magnacca, V. Boffa, T.D. Bennett, Y. Yue, Polymorph formation for a zeolitic imidazolate framework composition - Zn(Im) 2, Microporous Mesoporous Mater. 265 (2018) 57–62. https://doi.org/10.1016/j.micromeso.2018.01.038.

[38] D.A. Carter, J.E. Pemberton, Raman spectroscopy and vibrational assignments of 1- and 2-methylimidazole, J. Raman Spectrosc. 28 (1997) 939–946. https://doi.org/10.1002/(SICI)1097-4555(199712)28:12<939::AID-JRS186>3.0.CO;2-R.

[39] G. Kumari, K. Jayaramulu, T.K. Maji, C. Narayana, Temperature Induced Structural Transformations and Gas Adsorption in the Zeolitic Imidazolate Framework ZIF-8: A Raman Study, J. Phys. Chem. A. 117 (2013) 11006–11012. https://doi.org/10.1021/jp407792a.

[40] L.M. Markham, L.C. Mayne, B.S. Hudson, M.Z. Zgierski, Resonance Raman studies of imidazole, imidazolium, and their derivatives: the effect of deuterium substitution, J. Phys. Chem. 97 (1993) 10319–10325. https://doi.org/10.1021/j100142a010.

[41] J.-C. Tan, B. Civalleri, A. Erba, E. Albanese, Quantum mechanical predictions to elucidate the anisotropic elastic properties of zeolitic imidazolate frameworks: ZIF-4 vs. ZIF-zni, CrystEngComm. 17 (2015) 375–382. https://doi.org/10.1039/C4CE01564A.

[42] D.W. Lewis, A.R. Ruiz-Salvador, A. Gómez, L.M. Rodriguez-Albelo, F.X. Coudert, B. Slater, A.K. Cheetham, C. Mellot-Draznieks, Zeolitic imidazole frameworks: Structural and

energetics trends compared with their zeolite analogues, CrystEngComm. 11 (2009) 2272–2276. https://doi.org/10.1039/b912997a.

[43] J.C. Tan, T.D. Bennett, A.K. Cheetham, Chemical structure, network topology, and porosity effects on the mechanical properties of Zeolitic Imidazolate Frameworks, Proc. Natl. Acad. Sci. 107 (2010) 9938–9943. https://doi.org/10.1073/pnas.1003205107.

[44] Y.-S. Li, H. Bux, A. Feldhoff, G.-L. Li, W.-S. Yang, J. Caro, Controllable Synthesis of Metal-Organic Frameworks: From MOF Nanorods to Oriented MOF Membranes, Adv. Mater. 22 (2010) 3322–3326. https://doi.org/10.1002/adma.201000857.

[45] M. Naseri, F. Pitzalis, C. Carucci, L. Medda, L. Fotouhi, E. Magner, A. Salis, Lipase and Laccase Encapsulated on Zeolite Imidazolate Framework: Enzyme Activity and Stability from Voltammetric Measurements, ChemCatChem. 10 (2018) 5425.

[46] K.S. Park, Z. Ni, A.P. Côté, J.Y. Choi, R. Huang, F.J. Uribe-Romo, H.K. Chae, M. O'Keeffe, O.M. Yaghi, Exceptional chemical and thermal stability of zeolitic imidazolate frameworks, Proc. Natl. Acad. Sci. U. S. A. 103 (2006) 10186–10191. https://doi.org/10.1073/pnas.0602439103.

[47] R. Ricco, P. Wied, B. Nidetzky, H. Amenitsch, P. Falcaro, Magnetically responsive horseradish peroxidase@ZIF-8 for biocatalysis, Chem. Commun. 56 (2020) 5775–5778. https://doi.org/10.1039/c9cc09358c.

[48] K. Liang, R. Ricco, C.M. Doherty, M.J. Styles, S. Bell, N. Kirby, S. Mudie, D. Haylock, A.J. Hill, C.J. Doonan, P. Falcaro, Biomimetic mineralization of metal-organic frameworks as protective coatings for biomacromolecules, Nat. Commun. 6 (2015) 7240. https://doi.org/10.1038/ncomms8240.

[49] W. Liang, F. Carraro, M.B. Solomon, S.G. Bell, H. Amenitsch, C.J. Sumby, N.G. White, P.

Falcaro, C.J. Doonan, Enzyme encapsulation in a porous hydrogen-bonded organic framework, J. Am. Chem. Soc. 141 (2019) 14298–14305. https://doi.org/10.1021/jacs.9b06589.

[50] W. Liang, R. Ricco, N.K. Maddigan, R.P. Dickinson, H. Xu, Q. Li, C.J. Sumby, S.G. Bell, P. Falcaro, C.J. Doonan, Control of Structure Topology and Spatial Distribution of Biomacromolecules in Protein@ZIF-8 Biocomposites, Chem. Mater. 30 (2018) 1069–1077. https://doi.org/10.1021/acs.chemmater.7b04977.

[51] J.B. James, Y.S. Lin, Kinetics of ZIF-8 Thermal Decomposition in Inert, Oxidizing, and Reducing Environments, J. Phys. Chem. C. 120 (2016) 14015–14026. https://doi.org/10.1021/acs.jpcc.6b01208.

[52] W. Liang, P. Wied, F. Carraro, C.J. Sumby, B. Nidetzky, C.-K. Tsung, P. Falcaro, C.J. Doonan, Metal–Organic Framework-Based Enzyme Biocomposites, Chem. Rev. 121 (2021) 1077–1129. https://doi.org/10.1021/acs.chemrev.0c01029.

[53] K.I. Hadjiivanov, D.A. Panayotov, M.Y. Mihaylov, E.Z. Ivanova, K.K. Chakarova, S.M. Andonova, N.L. Drenchev, Power of Infrared and Raman Spectroscopies to Characterize Metal-Organic Frameworks and Investigate Their Interaction with Guest Molecules, Chem. Rev. 121 (2021) 1286–1424. https://doi.org/10.1021/acs.chemrev.0c00487.

[54] R.C. Feldhoff, T. Peters, Fragments of bovine serum albumin produced by limited proteolysis. Isolation and characterization of peptic fragments, Biochemistry. 14 (1975) 4508–4514. https://doi.org/10.1021/bi00691a027.

[55] R. Lu, W.-W. Li, A. Katzir, Y. Raichlin, H.-Q. Yu, B. Mizaikoff, Probing the secondary structure of bovine serum albumin during heat-induced denaturation using mid-infrared fiberoptic sensors, Analyst. 140 (2015) 765–770. https://doi.org/10.1039/C4AN01495B.

[56] Z. He, Z. Liu, X. Zhou, H. Huang, Low pressure-induced secondary structure transitions of regenerated silk fibroin in its wet film studied by time-resolved infrared spectroscopy, Proteins Struct. Funct. Bioinforma. 86 (2018) 621–628. https://doi.org/10.1002/prot.25488.

[57] D. Badillo-Sanchez, D. Chelazzi, R. Giorgi, A. Cincinelli, P. Baglioni, Understanding the structural degradation of South American historical silk: A Focal Plane Array (FPA) FTIR and multivariate analysis, Sci. Rep. 9 (2019) 17239. https://doi.org/10.1038/s41598-019-53763-5.